Solid Freeform Fabrication 2018: Proceedings of the 29th Annual International Solid Freeform Fabrication Symposium – An Additive Manufacturing Conference
Reviewed Paper

SIMULATION OF THE THERMAL BEHAVIOR AND ANALYSIS OF SOLIDIFICATION PROCESS DURING SELECTIVE LASER MELTING OF ALUMINA

Kai Zhang*, Tingting Liu*, Wenhe Liao*, Changdong Zhang*, Yi Zheng*, Huang Shao*

* School of Mechanical Engineering, Nanjing University of Science and Technology, Nanjing, 210094, China

Abstract

Selective laser melting (SLM) has rapidly developed in the past decade. High precision-complex ceramics parts can be directly fabricated using this technology. To study the thermal behavior of molten pools in the selective laser melting of alumina （Al_2O_3）, we established a three-dimensional model based on ANSYS. Then, combined with simulation results, the physical phenomena during the rapid solidification process were discussed. The simulation results showed that the laser power and scanning speed exerts a marked influence on the maximum temperature, liquid lifetime, dimensions, and temperature gradient of the molten pool. Owing to the different temperature gradients in the molten pool, the thermal capillary force on the free surface varies. As a result, a slight difference exists between the stripy solidification structures. Different orientations of columnar crystals can be obtained. The underlying mechanism controls the direction of the temperature gradient with suitable processing routes, such as decreasing the scanning speed.

Introduction

Selective laser melting is an additive manufacturing technique that has rapidly developed over the past decade [1, 2]. This manufacturing technology can fabricate complex parts without the time-consuming mold design process [3]. In terms of materials, metal and nylon/plastic have already been widely studied and applied commercially [4–6]. In recent years, the SLM of ceramics has garnered the interest of many researchers [7, 8].

Shishkovsky and Bertrand performed SLM on alumina–zirconium and zirconia to produce ceramic parts [9, 10]. Deckers investigated the electrophoretic deposition (EPD) layer of a sub-micrometer Al_2O_3 ceramic slurry and SLM at a high preheating temperature (800℃) [11]. Wilkes and Hagedorn investigated the SLM of Al_2O_3–ZrO_2 powder mixtures and demonstrated that crack-free ceramic objects can be manufactured by high-temperature (1600 °C) preheating [12–14]. Liu et al. studied the effect of high-temperature preheating on crack distribution [15, 16]. Owing to the high melting point and brittleness of ceramic, it is comparatively difficult to manufacture crack-free specimens by SLM. Therefore, further understanding of cracks needs to be developed. In fact, the temperature field has an important effect on the formation of cracks. However, it is difficult to directly measure the temperature field and the thermal behavior during SLM since it involves a rapid heating and cooling (up to 10^6K/s). Numerical simulation is considered effective for studying thermal behavior during SLM [17, 18].

In the past, many researchers have established heat conduction models to investigate the temperature distribution characteristics of molten pool during the process of SLM. Gusarov et al. studied the temperature field of stainless steel during SLM and found that scanning speed, powder thickness, and material thermal properties highly affect the stability of the process [19]. Gu et al. developed a finite element model to study the influences of laser power and scanning speed on the thermal behavior of commercially pure titanium and aluminum alloys during SLM [20, 21]. Verhaeghe presented a pragmatic engineering model to study the influence of incorporating or neglecting the effects of evaporation of Ti6Al4V during SLM and found that evaporation cannot be neglected [22]. Recently, Protasov showed that numerical modeling can predict the thermal behavior of fused silica during SLM [23]. Although certain numerical simulations had been conducted to investigate the temperature filed during SLM of metal powders, studies on ceramics are limited.

In this paper, the influences of laser power and scanning speed on temperature field of Al_2O_3 during SLM are first studied, because these two processing parameters are the most important factors which can directly control the thermal behavior. Then, combined with simulation results, directional solidification and thermocapillary convection which is induced by high temperature gradient during the rapid solidification process are discussed.

Model building

Basic equation of temperature

During SLM, the temperature gradient is large and the thermophysical properties of the materials are inconsistent. Therefore, the temperature field analysis of SLM belongs to the typical nonlinear transient thermal analysis problem, which can be expressed as:

$$\rho c \frac{\delta T}{\delta t} = \frac{\delta}{\delta x}\left(k \frac{\delta T}{\delta x}\right) + \frac{\delta}{\delta y}\left(k \frac{\delta T}{\delta y}\right) + \frac{\delta}{\delta z}\left(k \frac{\delta T}{\delta z}\right) + Q \tag{1}$$

Where ρ is the material density, c is the specific heat capacity, T is the temperature, t is the interaction time, k is the thermal conductivity, and $Q=(x, y, z)$ is the heat dissipation per unit volume.

The original state of the temperature field distribution at time t=0 can be expressed as follows:

$$T(x, y, z, 0) = T_0(x, y, z) \tag{2}$$

where T_0 is the preheating temperature, which was set to 400 K.

The boundary condition fits the follow equation:

$$-k\left[\frac{\partial T}{\partial z}\right]_{z=0} = Q - h(T_a - T_s) - \sigma\varepsilon(T_a^4 - T_s^4) \tag{3}$$

where T_a is the initial power bed temperature, T_s is the environment temperature, h is the heat convection coefficient, ε is the heat radiation coefficient, σ is Stefan–Boltzmann constant, and Q is the rate of heat flow.

Basic setting and assumptions

The SOLID70 heat unit was used to generate a mesh. With the accuracy and calculative rate of the temperature field analysis results simultaneously considered, this study used a small model as the analysis object. The size of the sample model was 1 mm × 1 mm × 0.05 mm, and the size of the mesh was 0.025 mm × 0.025 mm × 0.025 mm. The baseplate was fabricated from Al_2O_3, with a similar coefficient of thermal expansion as the Al_2O_3 parts manufactured by SLM, and the size of the baseplate was 1.4 mm × 1.4 mm × 0.5 mm. The baseplate was not the main analysis object; therefore, different volumes of mesh were selected for the baseplate. The upper part of the substrate was divided into 0.2 mm tetrahedron meshes, whereas the lower part of the substrate was divided into 0.4 mm hexahedron meshes. The entire model was composed of 6,172 nodes and 12,867 units, as shown in Fig. 1.

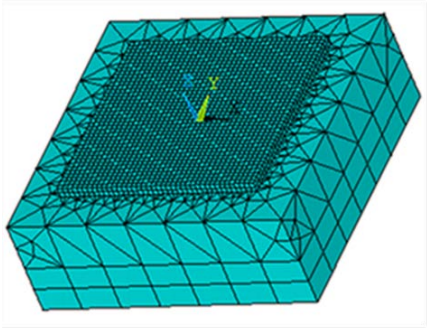

Fig. 1. Finite element model.

Basic assumptions of the model:

(1) The material is isotropic;

(2) The influence of the flow of molten pool to the temperature field is ignored;

(3) The absorptivity of Al_2O_3 powder to the laser energy is constant;

(4) The latent heat is negligible for the phase change;

(5) The effect of residual water on the thermal physical parameters and experimental process of the alumina powder is neglected. (Alumina slurry was used for experimental verification. Prior to laser processing, the slurry is preheated to approximately 400 K to remove excess water.)

Heat source model

The energy output distribution of the laser followed a nearly Gaussian distribution and can be described as follows:

$$I(r) = \frac{2AP}{\pi R^2} \exp\left(-\frac{2r^2}{R^2}\right) \tag{4}$$

where A is the absorbance of the powder system, P is the laser power, ω is the radius of the laser beam, and r is the distance between the point with the calculation of energy density and the beam center.

During the SLM process, the laser moved continuously along a specific path (without contour scanning), as shown in Fig. 2. During the simulation process, the continuous

movement was replaced by a discontinuous step, and every step was composed of two grids (50 μm), as shown in Fig. 3. The loading time of every step was determined by laser scanning speed, as follows:

$$time\ inc = \frac{size}{V} \tag{5}$$

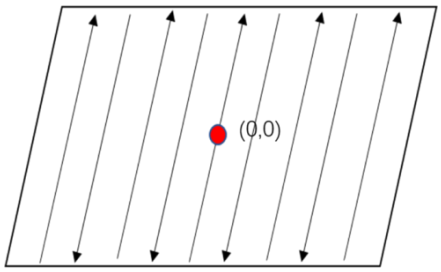

Fig. 2. Laser scanning pattern during SLM process

The laser spot action area was approximately circular, with the radius being twice the length of the grid (50 μm). The energy of the laser at each step affected 16 grids. After the current step was completed, the heat source was removed, and the current result of temperature was used as the initial condition of the next step. This process was cycled until the simulation was complete.

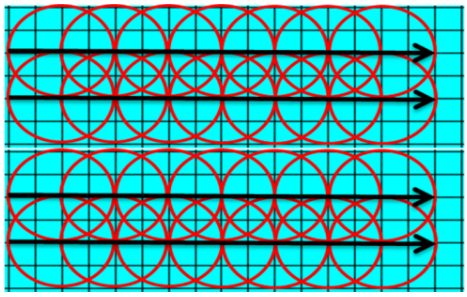

Fig. 3. Movement mode of the laser heat source.

Material properties

In this paper, the processing material is Al_2O_3. Its thermal physical parameters are in Tab. 1:

Tab. 1. Thermal physical parameters of Al_2O_3.

Temperature, T(K)	*300*	*600*	*1000*	*1700*	*2200*
Thermal conductivity, *k*(W/mK)	35	15.8	7.85	5.54	5.5
Specific heat capacity, c_p(J/kgK)	779	838	1224	1320	1330

Parameters of simulation process

The simulation process parameters are in Table 2. Laser power and scan speed are based on the previous experimental results [26]. The absorptivity of alumina is about 1.8% [28], but due to the influence of preheating temperature [29], so we assumption it is about 2.8%.

Tab. 2. Simulation parameters.

Parameter	*Value*
Absorptivity	0.028
Laser spot size, μm	100
Preheating temperature, K	400
Hatching spacing, μm	50
Layer thickness, μm	50
Laser power, W	100, 120, 140, 160, 180, 200
Scanning speed, mm/s	60, 70, 80, 90, 100, 110, 120

Experimental conditions

A laboratory-scale SLM system for ceramic was designed and built for the investigations. The SLM system is shown in Fig. 7. The machine was equipped with an IPG YLR-500 fiber laser, which produced a laser beam with a wavelength of 1070 nm and can reach a maximum power of 500 W in continuous mode. The laser was led through a scanner (intelliSCAN 20, SCANLAB, Germany). The spot size of the focused laser beam was approximately 60 μm. Moreover, the system was integrated with a 20 kW induction heating system (Shanghai Bamac, China). An Al_2O_3 baseplate (17.5 mm × 17.5 mm × 5 mm) was utilized in this experiment.

Fig. 4. Laboratory-scale SLM system.

Al_2O_3 slurry was prepared using an electromagnetic mixer at a mass ratio of 1:1 of Al_2O_3 powders (CT3000 SG, ALMTIS, China) and deionized water because this slurry presented good flow ability during layer deposition. A rubber scraper was used to layer the Al_2O_3 slurry. Finally, the substrate was preheated to approximately 110 °C to vaporize the water before SLM.

An infrared thermal imager (A615, FLIR, USA) was used to detect the temperature of Al_2O_3 during SLM.

Results

Comparison of simulation temperature and actual temperature

Figure 5 shows the maximum simulation temperatures and the maximum actual temperatures with time at 100 W and 90 mm/s. The results showed that the temperature of infrared thermal imager was virtually consistent with the temperature of the numerical

simulation. Moreover, the temperature changed cyclically and increased gradually during the SLM process because heat produced from the previous point or track affected the next point or track, thereby resulting heat accumulation during SLM.

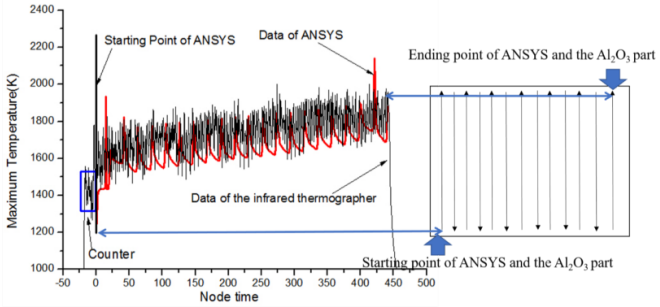

Fig. 5. The maximum simulation temperatures and the maximum actual temperatures with time at 100 W and 90 mm/s.

Basic temperature characteristics of molten pool

Figure 6 shows the maximum temperature and lifetime of the molten pool at the point (0, 0) with different laser powers (a) and scanning speeds (b). When the scanning speed is 90 mm/s and the laser power increased from 100 W to 200 W, the maximum temperature of the molten pool increased monotonously from 1619.02 K to 3276.79 K. The results indicated that Al_2O_3 melted with the laser power of 160, 180, and 200W. The liquid lifetimes of the molten pool were 0.13 ms, 0.27 ms and 0.4 ms. When the scanning speed increased from 60 mm/s to 100 mm/s, the maximum temperature of the molten pool decreased from 2754.45 K to 1980.59 K. This finding indicated that Al_2O_3 can be melted by reducing the scanning speed, such as decreasing the scanning speed to 80, 70, or 60 mm/s and fixing the laser power at 140 W. Moreover, the liquid lifetimes of the molten pool were 0.04 ms, 0.14 ms and 0.26 ms.

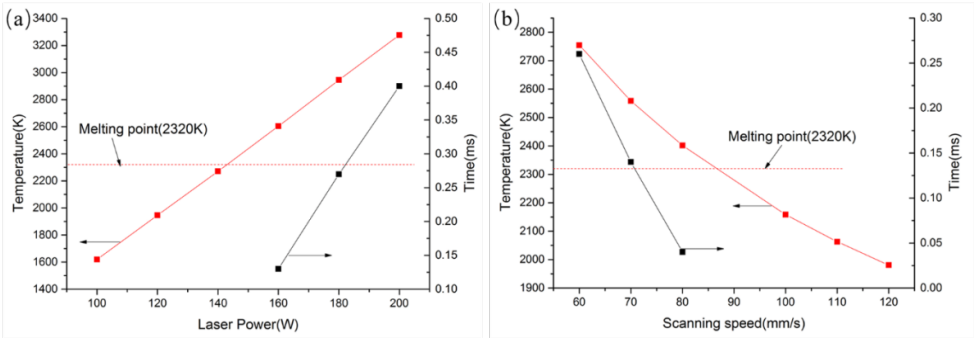

Fig. 6. Maximum temperature and lifetime of the molten pool at the point (0, 0) with different laser powers (a) and scanning speeds (b).

Figure 7 depicts the effect of laser powers and scanning speeds on the length and width of molten pool during SLM of Al_2O_3 powder. The experimental results clearly show that the dimensions of the molten pool increased as the laser power increased or scanning speed decreased. With increasing laser power from 160 W to 200 W, the length of the molten pool increased from 38.8 μm to 74.44 μm. Meantime, the width of the molten pool increased from 21.44 μm to 53.73 μm. As the scanning speed increased from 60 mm/s to 80 mm/s, the length of the molten pool increased from 13.06 μm to 43.66 μm, and the width of the molten pool

increased from 7.19 μm to 30.88 μm.

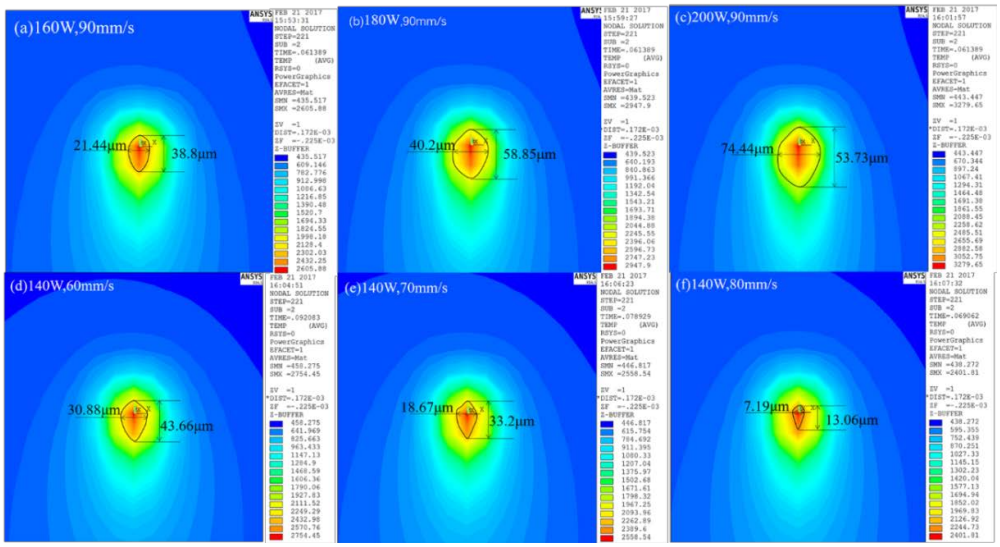

Fig. 7. The effect of laser powers and scanning speeds on the length and width of molten pool as the laser beam reached the point (0, 0) during SLM of Al_2O_3 powder. 160 W and 90 mm/s (a), 180 W and 90 mm/s (b), 200 W and 90 mm/s (c), 140 W and 60 mm/s (d), 140 W and 70 mm/s (e) and 140 W and 80 mm/s (f).

Basic characteristics of temperature gradient

Figure 8 shows the influence of laser powers and scanning speeds on the temperature gradient of the point (−25, 0) μm, which is close to the solidification edge of the molten pool, as the laser beam reached the point (0, 0) μm. When the laser power increased from 100 W to 200 W, the temperature gradient in the molten pool along the *x*, *y*, and *z* directions increased from 1.7922×10^7, 3.6545×10^6, and 2.2096×10^7 K/m to 4.3912×10^7, 1.2519×10^6, and 5.8942×10^7 K/m. When the scanning speed increased from 60 mm/s to 120 mm/s, the temperature gradient in the molten pool along the *x*, *y*, and *z* directions decreased from 3.5278×10^7, 8.4993×10^6, and 4.5608×10^7 K/m to 2.3739×10^7, 6.2608×10^6, and 3.0849×10^7 K/m. Comparison of the data in Figs. 8(a) and 8(b) revealed that the laser power exerted a higher effect than the scanning speed on the temperature gradient along the *x* and *z* directions.

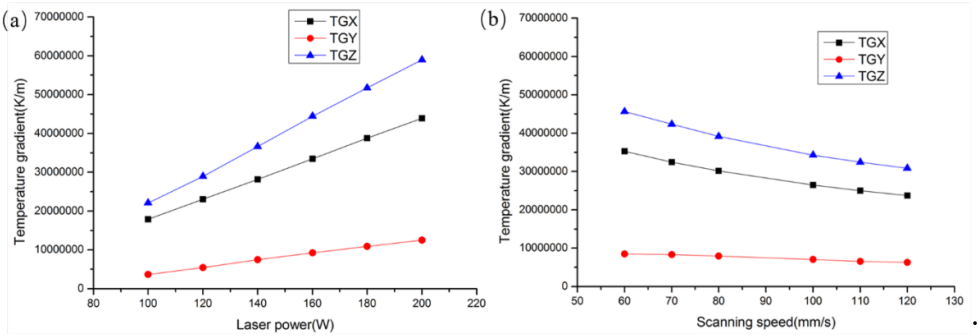

Fig. 8. Influence of laser powers and scanning speeds on the temperature gradient of the point (−25, 0) μm, which is close to the solidification edge of the molten pool, as the laser beam

reached the point (0, 0) μm.

Figure 9 shows the temperature gradient along the *x*-direction path at $y = 0$ μm. Apparently, the temperature gradient can be divided into three parts (A, B, and C). In region A, the temperature gradient in the *x* direction is larger than that in the *z* direction; in regions B and C, the temperature gradient in the *z* direction are larger than those in the *x* and *y* directions.

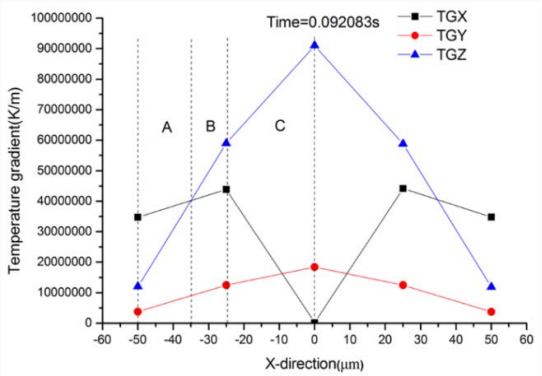

Fig. 9. Temperature gradient along the x-direction path at y=0 μm.

Figure 10 shows the ratio of the *x* and *y* directions of temperature gradients at the front of the solidification interface (the edge of molten pool) and at different scanning speeds (the precise coordinate locations of the solidification front are based on the data in Fig. 7). The figure shows that the temperature gradient in the *x* direction gradually strengthens with the decrease in scanning speed. At a scanning speed of 60 mm/s, the growth power at *x* direction became stronger than that in the *z* direction, and the columnar grains grew along the *x* direction.

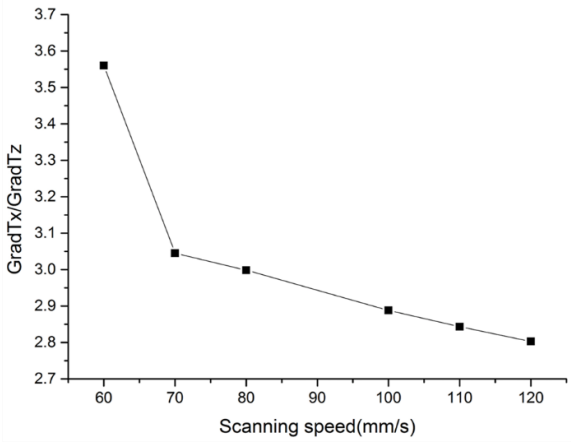

Fig. 10. Ratio of the *x* and *y* directions of the temperature gradient at the front of the solidification interface with different scanning speeds.

Discussion

Thermocapillary Convection

As seen in Fig. 11, a stripy solidification structure formed on the free surface along the

scanning direction of the laser. Careful observation revealed that the stripy solidification structure can be divided into three parts (A′, B′, and C′). Region A′ presented the most evident stripy solidification structure, followed by the region B′, and the structure virtually disappeared in the region C′. The Bernard flower model can explain the above phenomenon in detail [27]. In region C′, the vertical Marangoni effect was larger than the horizontal Marangoni effect; thereby resulting in a strong horizontal Marangoni effect driving the fluid toward the cold end. Moreover, the fluid stacking at the cold end induced deformation in the free surface. The molten pool existed for a short time (approximately 0.4 ms) and the deformation was too late to be restored; ultimately, a special surface coagulation tissue formed. In region B′, the temperature gradient in the *z*-direction was larger than that in the *x* and *y* directions (Fig. 9 region B) and a weak horizontal Marangoni effect drove the fluid toward the cold end, thereby resulting in small deformation and unseen stripy solidification structure. In region A′, the temperature gradient in the *x* direction was larger than that in the *z* direction (Fig. 9 region A), therefore, the upward convection vanished on the free surface.

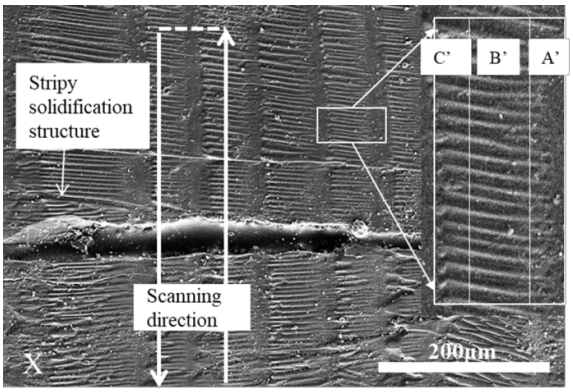

Fig. 11. Stripy solidification structure on the surface of a Al_2O_3 SLM specimen at 200 W and 90 mm/s.

Directional solidification

The crystallographic texture and solidification microstructure in SLM for metal have been studied by numerous scholars [24, 25]. The theoretical model of typical solidification microstructure of the molten pool in the process of SLM is shown in Fig. 12(a). Moreover, this typical solidification microstructure of the molten pool could be seen in SLM of Al_2O_3, as shown in Fig. 12(b). The figure shows two different directional solidification microstructures, namely, Zones I and II. This phenomenon may be associated with the change in temperature gradient at the front of the solidification interface (see Fig. 9) that induced the transformation of columnar grain growth. Crystal growth took place in the preferred direction closest to the heat flow direction. In Zone I, the temperature gradient mainly resided along the *z* direction; therefore, the solidification microstructure grew along the *z* direction from the bottom of the molten pool. However, in Zone II, the direction of the temperature gradient was shifted to the *x* direction, as shown in Fig. 9. The figure indicates that the direction of the solidification microstructure can be controlled with suitable processing routes.

Figure 13 shows the microstructure of the cross section of slurry deposition samples at different scanning speeds. At a lower scanning speed of 60 mm/s, the columnar grains mainly

grew along the *x* direction (Fig. 13(a)). Upon increasing the scanning speed to 120 mm/s, the columnar grains grew along the *z* direction (Fig. 13(b)). This result may be caused by the changing of temperature gradient. As shown in Fig. 10, the temperature gradient along the *x* direction was increased by the decreasing scanning speed. The direction of the solidification microstructure could be fully changed at the scanning speed of 60 mm/s. Therefore, the growth direction of the columnar grains could be adjusted by changing the scanning speed.

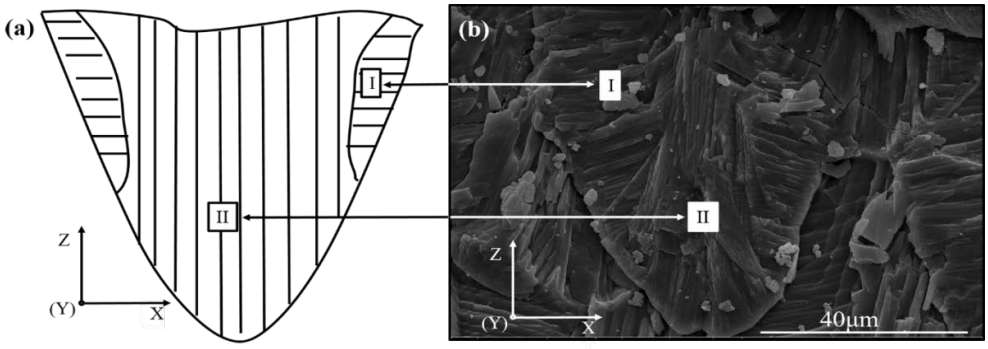

Fig. 12. Theoretical model of typical solidification microstructure of the molten pool in the SLM process (a) and the same solidification microstructure in the SLM of Al_2O_3 (b).

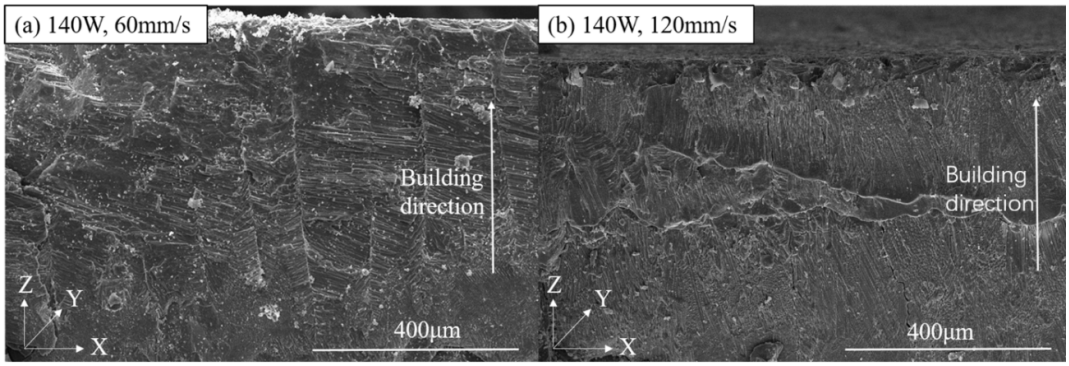

Fig. 13. Microstructure of the cross-section SEM images of SLM-processed Al_2O_3 samples showing the microstructure for a fixed laser power of 140 W and scanning speeds of 60 (a) and 120 mm/s (b).

Conclusion

A finite element model was built to investigate the effects of laser power and scanning speed on the temperature field of Al_2O_3 during SLM. Combined with the experiment, the simulation results were investigated, and thermocapillary convection and grain growth direction were discussed. The mainly conclusions were summarized:

(1) The temperature of infrared thermal imager was almost consistent with the temperature of the numerical simulation. Moreover, the temperature gradually increased during the SLM process because of the heat accumulation effect.

(2) The slight difference between stripy solidification structures can be explained by the different thermal capillary forces induced by the different temperature gradients. With a higher temperature gradient in the X-direction, the enhanced horizontal Marangoni effect

and the increasingly evident stripy solidification structure were observed.

(3) At a low scanning speed of 60 mm/s, the columnar grains of Al_2O_3 produced through SLM mainly grew along the *x* direction (perpendicular to the building direction). This finding indicated that the direction of the solidification microstructure can be controlled with suitable processing routes, such as decreasing the scanning speed.

The model is relatively simple and contains certain limiting assumptions; however, the model, when combined with experiments, still yielded conclusions with a certain degree of credibility. In the future, the model will be optimized to study the accurately thermal behavior of ceramics in the SLM process.

Acknowledgements

This work was supported by the National Natural Science Foundation of China (Grant No. 51375242), A Project Funded by the Priority Academic Program Development of Jiangsu Higher Education Institutions (PAPD) and National Key R&D Program of China (Grant No.2016YFB1100500-04).

References

[1] J.P. Kruth, G. Levy, F. Klocke, T.H.C. Childs, Consolidation phenomena in laser and powder-bed based layered manufacturing, CIRP Ann. - Manuf. Technol. 56 (2007) 730–759. doi:10.1016/j.cirp.2007.10.004.

[2] D.D. Gu, W. Meiners, K. Wissenbach, R. Poprawe, Laser additive manufacturing of metallic components: materials, processes and mechanisms, Int. Mater. Rev. 57 (2012) 133–164. doi:10.1179/1743280411Y.0000000014.

[3] W. Meiners, K. Wissenbach, A. Gasser, Selective laser sintering at melting temperature, U.S. Pat. 6215093. 1 (2001).

[4] C.Y. Yap, C.K. Chua, Z.L. Dong, Z.H. Liu, D.Q. Zhang, L.E. Loh, S.L. Sing, Review of selective laser melting: Materials and applications, Appl. Phys. Rev. 2 (2015). doi:10.1063/1.4935926.

[5] C. Teng, D. Pal, H. Gong, K. Zeng, K. Briggs, N. Patil, B. Stucker, A review of defect modeling in laser material processing, Addit. Manuf. 14 (2017) 137–147.

[6] B.P. Conner, G.P. Manogharan, A.N. Martof, L.M. Rodomsky, C.M. Rodomsky, D.C. Jordan, J.W. Limperos, Making sense of 3-D printing: Creating a map of additive manufacturing products and services, Addit. Manuf. 1 (2014) 64–76. doi:10.1016/j.addma.2014.08.005.

[7] S.L. Sing, W.Y. Yeong, F.E. Wiria, B.Y. Tay, Z. Zhao, L. Zhao, Z. Tian, S. Yang, Direct selective laser sintering and melting of ceramics: a review, Rapid Prototyping Journal, 2017. doi:10.1108/RPJ-11-2015-0178.

[8] I.H. Ahn, S.K. Moon, J. Hwang, G. Bi, Characteristic length of the solidified melt pool in selective laser melting process, Rapid Prototyp. J. 23 (2017). doi:10.1108/RPJ-06-2015-0076.

[9] I. Shishkovsky, I. Yadroitsev, P. Bertrand, I. Smurov, Alumina-zirconium ceramics synthesis by selective laser sintering/melting, Appl. Surf. Sci. 254 (2007) 966–970. doi:10.1016/j.apsusc.2007.09.001.

[10] P. Bertrand, F. Bayle, C. Combe, P. Goeuriot, I. Smurov, Ceramic components manufacturing by selective laser sintering, Appl. Surf. Sci. 254 (2007) 989–992. doi:10.1016/j.apsusc.2007.08.085.

[11] J. Deckers, S. Meyers, J.P. Kruth, J. Vleugels, Direct selective laser sintering/melting of high density alumina powder layers at elevated temperatures, Phys. Procedia. 56 (2014) 117–124. doi:10.1016/j.phpro.2014.08.154.

[12] Y. Hagedorn, Additive Manufacturing of High Performance Oxide Ceramics via Selective Laser Melting, 2013.

[13] H. Yves-Christian, W. Jan, M. Wilhelm, W. Konrad, P. Reinhart, Net shaped high performance oxide ceramic parts by Selective Laser Melting, Phys. Procedia. 5 (2010) 587–594. doi:10.1016/j.phpro.2010.08.086.

[14] J. Wilkes, Y.-C. Hagedorn, W. Meiners, W. Konrad, Additive manufacturing of ZrO2 Al2O3 ceramic components by selective laser melting, Rapid Prototyp. J. 19 (2013) 51–57. doi:10.1108/13552541311292736.

[15] Q. Liu, Y. Danlos, B. Song, B. Zhang, S. Yin, H. Liao, Effect of high-temperature preheating on the selective laser melting of yttria-stabilized zirconia ceramic, J. Mater. Process. Technol. 222 (2015) 61–74. doi:10.1016/j.jmatprotec.2015.02.036.

[16] Q. Liu, B. Song, H. Liao, Microstructure study on selective laser melting yttria stabilized zirconia ceramic with near IR fiber laser, Rapid Prototyp. …. 20 (2014) 2. doi:10.1108/RPJ-12-2012-0113.

[17] L.E. Loh, C.K. Chua, W.Y. Yeong, J. Song, M. Mapar, S.L. Sing, Z.H. Liu, D.Q. Zhang, Numerical investigation and an effective modelling on the Selective Laser Melting (SLM) process with aluminium alloy 6061, Int. J. Heat Mass Transf. 80 (2015) 288–300. doi:10.1016/j.ijheatmasstransfer.2014.09.014.

[18] O. Lopez-Botello, U. Martinez-Hernandez, J. Ramírez, C. Pinna, K. Mumtaz, Two-dimensional simulation of grain structure growth within selective laser melted AA-2024, Mater. Des. 113 (2017) 369–376. doi:10.1016/j.matdes.2016.10.031.

[19] A. V. Gusarov, I. Smurov, Modeling the interaction of laser radiation with powder bed at selective laser melting, Phys. Procedia. 5 (2010) 381–394. doi:10.1016/j.phpro.2010.08.065.

[20] Y. Li, D. Gu, Thermal behavior during selective laser melting of commercially pure titanium powder: Numerical simulation and experimental study, Addit. Manuf. 1 (2014) 99–109. doi:10.1016/j.addma.2014.09.001.

[21] D. Dai, D. Gu, Thermal behavior and densification mechanism during selective laser melting of copper matrix composites: Simulation and experiments, Mater. Des. 55 (2014) 482–491. doi:10.1016/j.matdes.2013.10.006.

[22] F. Verhaeghe, T. Craeghs, J. Heulens, L. Pandelaers, A pragmatic model for selective laser melting with evaporation, Acta Mater. 57 (2009) 6006–6012. doi:10.1016/j.actamat.2009.08.027.

[23] C.E. Protasov, R.S. Khmyrov, S.N. Grigoriev, A. V. Gusarov, Selective laser melting of fused silica: Interdependent heat transfer and powder consolidation, Int. J. Heat Mass Transf. 104 (2017) 665–674. doi:10.1016/j.ijheatmasstransfer.2016.08.107.

[24] L. Thijs, K. Kempen, J.P. Kruth, J. Van Humbeeck, Fine-structured aluminium products with controllable texture by selective laser melting of pre-alloyed AlSi10Mg powder, Acta Mater. 61 (2013) 1809–1819. doi:10.1016/j.actamat.2012.11.052.

[25] J. Liu, A.C. To, Quantitative texture prediction of epitaxial columnar grains in additive manufacturing using selective laser melting, Addit. Manuf. (2017). doi:10.1016/j.addma.2017.05.005.

[26] Kai Zhang, Tingting Liu, Wenhe Liao, et al. Influence of laser parameters on the surface morphology of slurry-based Al2O3 parts produced through selective laser melting[J]. Rapid Prototyping Journal, 2018,24(2):333-341.

[27] Pearson J R A. On convection cells induced by surface tension [J]. Journal of Fluid Mechanics, 1958, 4(5):489-500.

[28] J. Wilkes. Selektives Laserschmelzen zur generativen Herstellung von Bauteilen aus hochfester Oxidkeramik. Ph.D. thesis, RWTH-Aachen, 2009.

[29] Z. Zhang & M. Modest. Temperature-Dependent Absorptances of Ceramics for Nd:YAG and CO2 Laser Processing Applications. Journal of Heat and Mass Transfer, 120: (1998), 322–327.